RESEARCH ARTICLE

Observation of Refractive Index Line Shape in Ultrafast XUV Transient Absorption Spectroscopy

Mingze Sun[1,2†], Zixiang Jiang[1,2†], Yong Fu[3†], Yanrong Jiang[1,2], Hongtao Hu[4], Chunyuan Bai[1,2], Zhongyao Yue[1,2], Jiaming Jiang[1,2], Hongqiang Xie[5], Cheng Jin[3*], Ruxin Li[1,6], P. B. Corkum[7,8], D. M. Villeneuve[7,8], and Peng Peng[1,2*]

[1]School of Physical Science and Technology, ShanghaiTech University, Shanghai 201210, Shanghai, China. [2]Center for Transformative Science, ShanghaiTech University, Shanghai 201210, Shanghai, China. [3]Department of Applied Physics, Nanjing University of Science and Technology, Nanjing, Jiangsu 210094, China. [4]Photonics Institute, Technische Universität Wien, A-1040 Vienna, Austria. [5]School of Science, East China University of Technology, Nanchang, Jiangxi, China. [6]State Key Laboratory of High Field Laser Physics, Shanghai Institute of Optics and Fine Mechanics, Chinese Academy of Sciences, Shanghai 201800, Shanghai, China. [7]Joint Attosecond Science Laboratory, National Research Council and University of Ottawa, 100 Sussex Drive, Ottawa, ON K1A 0R6, Canada. [8]Department of Physics, University of Ottawa, 25 Templeton St., Ottawa, ON K1N 6N5, Canada.

*Address correspondence to: cjin@njust.edu.cn (C.J.); pengpeng@shanghaitech.edu.cn (P.P.)
†These authors contributed equally to this work.

Ultrafast extreme ultraviolet (XUV) transient absorption spectroscopy measures the time- and frequency-dependent light losses after light–matter interactions. In the linear region, the matter response to an XUV light field is usually determined by the complex refractive index $\tilde{n}$. The absorption signal is directly related to the imaginary part of $\tilde{n}$, namely, the absorption index. The real part of $\tilde{n}$ refers to the real refractive index, which describes the chromatic dispersion of an optical material. However, the real refractive index information is usually not available in conventional absorption experiments. Here, we investigate the refractive index line shape in ultrafast XUV transient absorption spectroscopy by using a scheme that the XUV pulse traverses the target gas jet off-center. The jet has a density gradient in the direction perpendicular to the gas injection direction, which induces deflection on the XUV radiation. Our experimental and theoretical results show that the shape of the frequency-dependent XUV deflection spectra reproduces the refractive index line profile. A typical dispersive refractive index line shape is measured for a single-peak absorption; an additional shoulder structure appears for a doublet absorption. Moreover, the refractive index line shape is controlled by introducing a later-arrived near-infrared pulse to modify the phase of the XUV free induction decay, resulting in different XUV deflection spectra. The results promote our understanding of matter-induced absorption and deflection in ultrafast XUV spectroscopy.

Introduction

The development of attosecond extreme ultraviolet (XUV) pulses based on high-harmonic generation has opened new possibilities for studying ultrafast physical, chemical, and biological processes with unprecedented time resolution [1–28]. The broad bandwidth and short duration of attosecond pulses are ideal for transient absorption measurements, resulting in the new technique: attosecond transient absorption spectroscopy (ATAS) [7–26]. Pump-probe type ATAS experiments that combine an attosecond pulse and a near-infrared (NIR) pulse have observed subcycle ac Stark shifts [15], states coupling effect [16], the generation of virtual states [17], and the vibrational and rotational motions in molecules [18–22].

As the present attosecond XUV pulses are weak, the light–matter interactions typically involve only 1 XUV photon (linear process in XUV) [3,4]. In this case, the matter response to an XUV light field is usually determined by the complex refractive index $\tilde{n}(\omega) = n(\omega) + i\beta(\omega)$, where ω is frequency, n is the real refractive index, and β is the absorption index. In general, n describes the incident light's phase shift, whereas β describes to its attenuation. The frequency dependence of β is related to the frequency-dependent absorption losses, i.e., the absorption line shape, which can be measured over a large spectral range. The frequency dependence of refractive index n describes the chromatic dispersion of an optical material, which is important for understanding the reflection and refraction of a laser field.

The conventional ATAS experiment uses a static flush gas cell to deliver the absorbing medium to the interaction region. The XUV pulse traverses the gas medium from the center, and the XUV spectrometer measures the transmitted XUV spectrum, by which the frequency-dependent absorption losses (β line shape) can be retrieved [8,9,21,23]. The refractive index line shape, however, is difficult to be obtained directly in such an experimental scheme. It was reported that when the XUV pulse crosses a density-gradient gas media, the angular dispersion on the XUV radiation was observed, and hence, the deflection and focusing of the XUV pulses can be realized [24].

The direction and magnitude of the XUV deflection angle depend on the refractive index n; thus, the frequency-dependent deflection spectrum may reflect the refractive index line shape. Moreover, the absorption line shape (β line shape) can be controlled experimentally; previous ATAS studies have revealed the laser-controlled absorption line shapes in helium [8,9,23] and the rotational coherence-controlled absorption line shapes in hydrogen and deuterium molecules [21]. n and β are not independent because they both describe the same process: the polarization of the material caused by the incident XUV pulse. Mathematically, n and β are connected with each other by Kramers–Kronig relations, $n(\omega) = 1 + \frac{2}{\pi} P \int_0^\infty \frac{\omega' \beta(\omega')}{\omega'^2 - \omega^2} d\omega'$, $\beta(\omega) = -\frac{2\omega}{\pi} P \int_0^\infty \frac{n(\omega') - 1}{\omega'^2 - \omega^2} d\omega'$, where P corresponds to the Cauchy principal value of the integral [29,30]. When the β line shape changes, the refractive index n line shape also changes accordingly. Until now, a comprehensive study of refractive index line shape in ATAS is basically lacking.

Here, we measure the refractive index line shape in helium. Based on the fact that the refractive index changes drastically at the atomic resonances and the XUV pulse is deflected spatially by the inhomogeneity of a gas jet [24], we show that the frequency-dependent XUV deflection spectra well reproduce the refractive index line shapes. For a single-peak discrete absorption with a typical Lorentzian profile, a dispersive n line shape is observed. For a doublet absorption structure, an additional shoulder-like feature appears on the deflection spectrum. The n line shape was further controlled by adding a NIR pulse after the XUV pulse. The NIR-induced Stark effect modifies the phase of the free induction decay (FID), resulting in a different absorption/refractive index line shape. Such effects were measured experimentally and agree well with the theoretical predictions. The results promote our understanding of matter-induced absorption and deflection in ultrafast XUV spectroscopy.

Materials and Methods

In the experiment, a Ti:sapphire laser system was used to produce the NIR laser pulses (100 Hz, 14 mJ, 800 nm, 50 fs). Approximately 1.6 mJ was sent into a gas-filled (0.7 bar of argon) hollow core fiber (250−μm inner diameter), and the pulse energy at the outlet of the fiber is 0.8 mJ. After multiple reflections of the chirp mirrors, the compressed pulse is 0.5 mJ at 10 fs. This pulse was used to generate high-order harmonic from a pulsed gas jet of xenon. We used a thin (80 ± 10 μm) monocrystalline quartz plate to further broaden the spectrum of the driving NIR pulse. The quartz plate was placed about 2 cm before the xenon gas jet and experienced a laser intensity of around 3×10^{13} W/cm^2 [21,22]. This intensity was strong enough to generate new spectral components through self phase modulation, but below the damage threshold ($>4 \times 10^{13}$ W/

cm^2) [27,28]. We used a 500-μm-diameter pinhole and 2 silicon mirrors to attenuate the NIR driving field. An intensity of 2×10^{11} W/cm^2 was estimated for the residual NIR pulse at the sample target based on the Stark shift. A toroidal mirror was used to refocus the XUV pulse into an absorption gas jet. The transmitted XUV spectrum was measured by a home-built XUV spectrometer.

A 3-dimensional manipulator was used to change the position of the absorption gas jet. The vertical distance from the XUV focus to the center of the gas jet is denoted as y; $y = 0$ means the XUV pulse traverses the gas jet through the center, while $y > 0$ means the XUV pulse is above the center. The gas jet has a density gradient in the vertical direction, which induces angular dispersion and deflection when the XUV pulse is below/above the center of the gas jet, i.e., the gas jet acts like a prism in the XUV range [24].

For the delay-dependent measurements, a 100-nm-thick sheet of aluminum foil was used to totally block the residual driving pulse. An 800-nm, 50-fs NIR pulse was picked off from the original pulse and used as the control pulse. The intensity of the NIR control pulse is ~1×10^{12} W/cm^2, and it was combined with the XUV pulse with a holey mirror. The XUV and the NIR pulses propagated noncollinearly and intersected at the absorption gas jet with a crossing angle of 18 mrad. The time delay between the XUV and the NIR pulses was precisely monitored by a motorized translation stage, and negative delay means the XUV pulse arrives before the NIR pulse. The broadband XUV pulse excites electronic coherences in helium, leading to FID that can last for picoseconds. The temporally overlapped or later-arrived NIR pulse induces an additional phase to the FID, resulting in a different line shape.

Results and Discussion

Figure 1A shows the experimental result for $y = -0.1$ mm. The broadband XUV pulse excites transitions from the ground state $1s^2$ to 1snp excited states of He, which results in attenuation of the transmitted spectrum at certain energies. Owing to the limited energy resolution of the XUV spectrometer (50 meV around 20 eV), we can only resolve absorption structures corresponding to 1snp resonances with $n = 2, 3, 4$, and 5. The deflection direction of the XUV spectrum below the 1snp resonances is upwards, while for the spectrum above these resonances, the deflection is downwards. This result reproduces the previous result reported by Drescher et. al. [24].

We further measured the transmitted XUV spectrum at different He gas jet positions. The results are shown in Fig. 1B and C. For $y = 0$ mm, the transmitted XUV spectrum is almost undeflected (the deflection angle is much smaller when compared with the case of $y = -0.1$ mm). The spectral dependence of the line shape near the resonant energies is probably induced by a small deflection, which can be caused by a misalignment of the gas jet center to the XUV beam center. The gas jet nozzle size is 100 μm, and the XUV beam size is 50 μm. During the experiments, we controlled the gas jet position (y) with a precision of 10 μm. For the $y = 0$ mm case, the center of the gas jet may not be perfectly aligned with the center of the XUV beam. Furthermore, the pulsed gas jet was used at a repetition rate of 100 Hz. Mechanical vibration is inevitable during experiments, which may change the gas jet position a bit, resulting in a small deviation. Figure 1C shows the result for $y = 0.1$ mm;
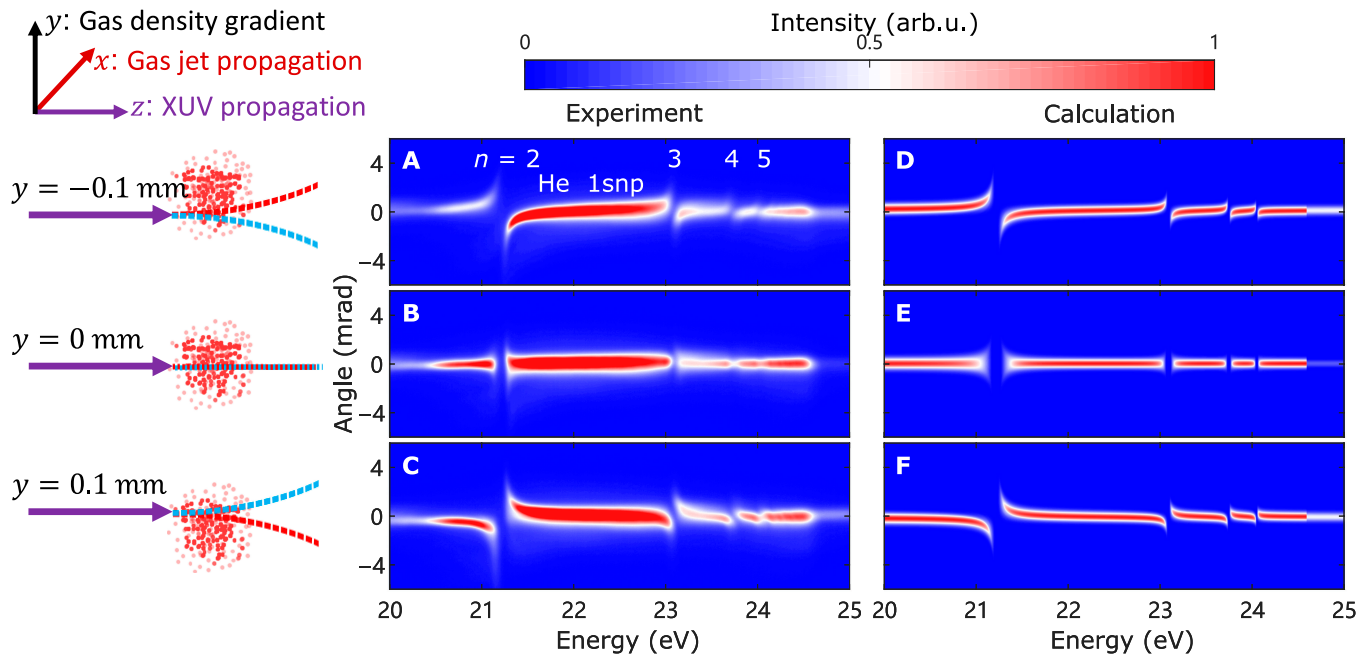
Fig. 1. Transmitted XUV spectrum at different He gas jet positions. The vertical distance from XUV focus to the center of the gas jet is denoted as y, the gas jet propagation direction is x, and the XUV propagation direction is z. (A) $y = -0.1$ mm, i.e., the XUV beam is 0.1 mm below the center of the He gas jet (backing pressure ~ 3 bar). The deflection direction of the XUV spectrum below the 1snp resonances is upwards, while for the spectrum above these resonances, the deflection is downwards. (B) $y = 0$, the XUV beam crosses the center of the He gas jet, and the transmitted XUV spectrum is undeflected. (C) $y = 0.1$ mm, the XUV beam is 0.1 mm above the center of the gas jet. The deflection direction of the XUV spectrum below the 1snp resonances is downwards, while for the spectrum above these resonances, the deflection is upwards. Simulation results are shown in (D) ($y = -0.1$ mm), (E) ($y = 0$ mm), and (F) ($y = 0.1$ mm).

on the contrary to the $y = -0.1$ mm case, the spectrum below (above) the resonances are deflected downwards (upwards).

The XUV deflection caused by the inhomogeneous gas jet is mainly determined by the refractive index. To simulate the deflection spectrum, we used the model described in [24]. The complex refractive index $\tilde{n}$ was calculated by the Lorentz–Lorenz formula [31].

$$\frac{\tilde{n}^2 - 1}{\tilde{n}^2 + 2} = N(y) \frac{e^2}{3m_e\epsilon_0} \sum_j \frac{f_j}{\omega_{0j}^2 - \omega^2 - i\Gamma_j\omega} \quad (1)$$

where $N(y) = N_0 e^{-\frac{y^2}{d^2}}$ is the spatial-dependent atomic density (we assume a Gaussian spatial profile, N_0 is the peak density of the gas jet, $d = 100$ μm is the nozzle size), e is the electron charge, m_e is the electron mass, ϵ_0 is the vacuum permittivity, f_j is the oscillator strength of the transition j, ω_{0j} is the resonant frequency, ω is the angular frequency of the XUV pulse, and Γ_j is the resonant width [32,33]. The real refractive index n and the absorption index β were calculated by $n = Re(\tilde{n})$, $\beta = Im(\tilde{n})$. We used the measured continuum absorption of helium to estimate the gas density. For the backing pressure of 3 bar, the peak density in the interaction region is estimated as $N_0 \sim 1.5 \times 10^{19}$ atoms/cm^3. We considered the 1snp resonances of He, $n = 2, 3, 4, 5$, and calculated the frequency (ω)- and spatial (y)-dependent complex refractive index $\tilde{n}(\omega, y)$ by using Eq. 1. The real and imaginary parts of $\tilde{n}(\omega, y)$, corresponding to the refractive index $n(\omega, y)$ and absorption index $\beta(\omega, y)$, respectively, are shown in Fig. 2 (the horizontal axis denotes the photon energy [frequency ω], and the right vertical axis denotes the spatial position y). Figure 2A shows that the
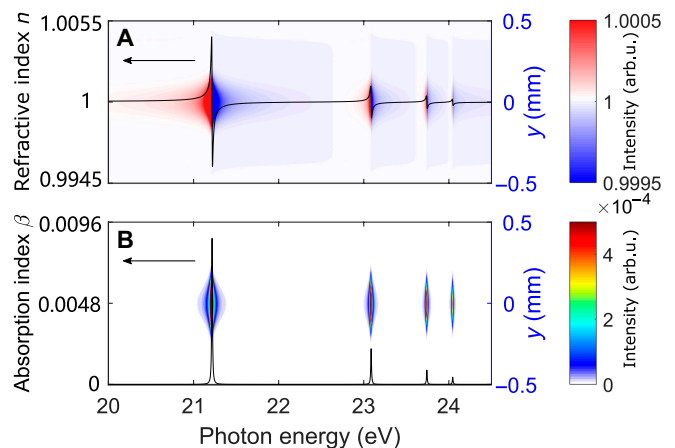

Fig. 2. Calculated refractive index n and absorption index β. (A) The black curve shows the calculated refractive index n at the center of the gas medium ($y = 0$, gas density $N_0 \sim 1.5 \times 10^{19}$ atoms/cm^3), a typical dispersive line shape can be seen in the vicinity of 1snp resonances ($n = 2, 3, 4, 5$). (B) The black curve is the absorption index β for the peak density N_0, which shows a Lorentzian line shape. The pseudo-color images are the frequency (ω)- and spatial (y)-dependent refractive index [$n(\omega, y)$, (A)] and absorption index [$\beta(\omega, y)$, (B)] when considering the y-dependent atomic density $N(y) = N_0 e^{-\frac{y^2}{d^2}}$.

refractive index $n > 1$ (indicated in red) at photon energies below the resonance, and $n < 1$ (indicated in blue) at photon energies above the resonance. We further extracted the refractive index at the center of the gas medium ($y = 0$, black curve in Fig. 2A), and a typical dispersive line shape can be seen.

Figure 2B shows the calculated absorption index β, which shows a symmetric Lorentzian profile.

The amplitude and phase changes of the XUV field was calculated by using the eikonal approximation, $A(y, z = 0) = A_0(y)e^{\frac{\omega L\{i[n(y)-1]-\beta(y)\}}{c}}$, where A_0 is the initial amplitude of the incident XUV field, $L = 0.2$ mm is the gas jet thickness, and c is the speed of light. The angle-dependent XUV amplitudes were calculated by applying the small-angle approximation of Kirchhoff diffraction formula, $\tilde{A}(\theta, z = S) \propto \int A(y)e^{i\omega\left[y\sin(\theta)+\frac{y^2}{2S}\right]/c} dy$, where $S = 1$ m is the

distance from the detector plane to the gas jet. A detailed description of the calculation model was provided by Drescher et al. in [24]. The simulation results are shown in Fig. 1D to F, which agree with the experimental results very well.

We now fix the gas jet at $y = -0.1$ mm and change the He backing pressure. The results for 1s2p resonance are shown in Fig. 3. Similar to the previous results reported in [24], the deflection increases with the backing pressure (Fig. 3A to C) as the refractive index gradient is proportional to the atomic density. Moreover, a narrow feature with small deflection can be seen at high pressures (Fig. 3B and C); such effect was not observed in [24].
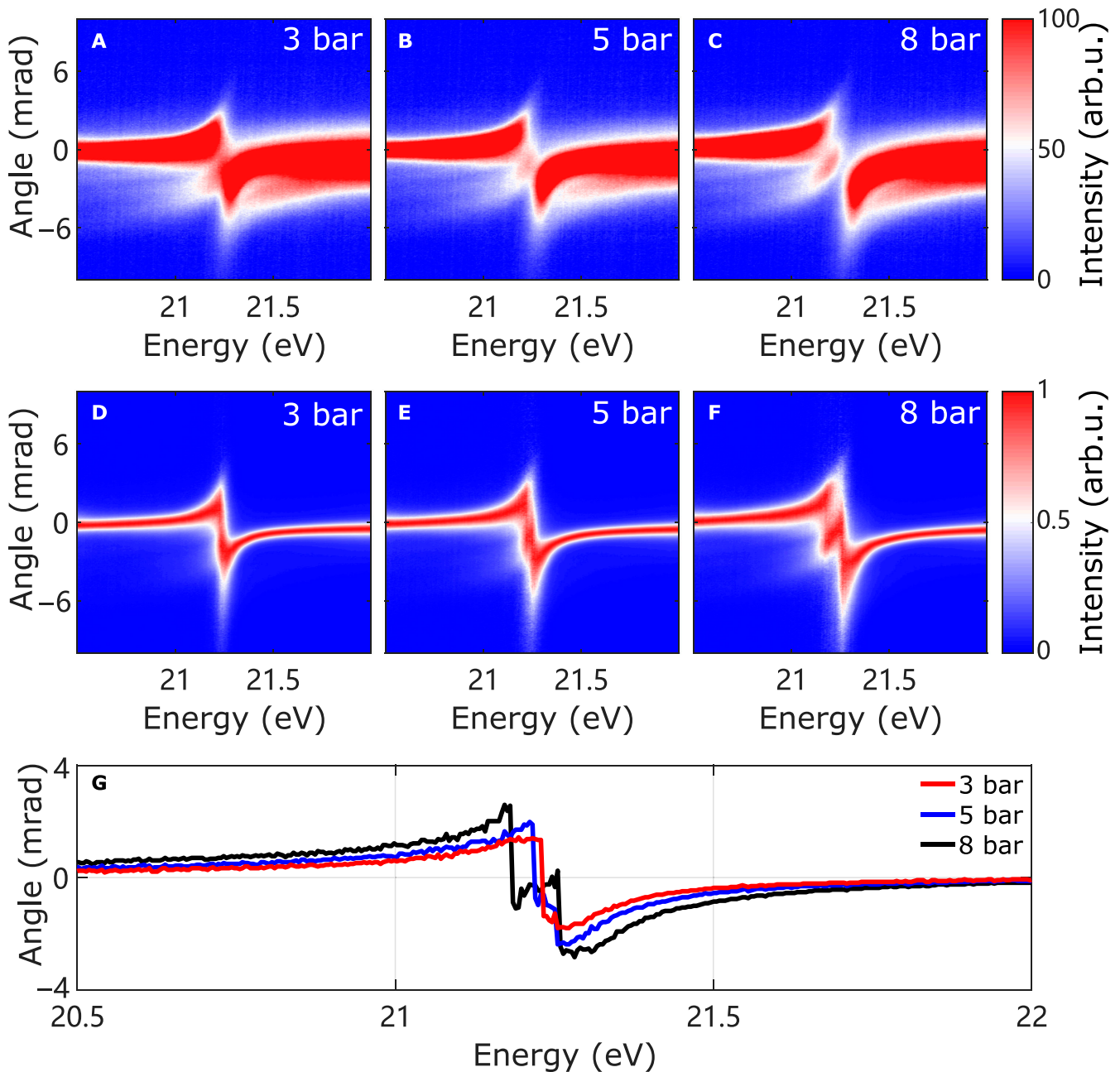

Fig. 3. Experimentally measured XUV deflection at different gas pressures. (A to C) XUV deflection spectra for backing pressures of 3 bar (A), 5 bar (B), and 8 bar (C), the gas jet was fixed at $y = -0.1$ mm. A narrow feature with small deflection can be seen at high pressures. (D to F) XUV spectra after applying intensity normalization along the deflection angle axis. (G) The deflection angle at the maximum intensity as a function of photon energy. The deflection has a typical dispersive line shape at 3 bar, while an additional shoulder structure appears at 5 bar; the shoulder structure becomes more obvious when the pressure increases to 8 bar.

For a better view of the narrow feature, we apply intensity normalization along the deflection angle axis (vertical axis), $I_{nor}(\omega,\theta) = I(\omega,\theta)/I_{max}(\omega)$, where $I_{nor}(\omega,\theta)$ is the normalized XUV spectrum, as shown in Fig. 3D to F; $I(\omega,\theta)$ is the measured XUV spectrum, as shown by Fig. 3A to C; and $I_{max}(\omega)$ is the maximum spectral intensity at each photon energy ω. For 3 bar, the deflection has a dispersive line shape, which is similar to the refractive index n in Fig. 2A. For 5 bar, the deflection shows an additional feature on the dispersive line shape. We call it the shoulder structure based on the shape; this structure becomes more obvious at 8 bar. We further extracted the deflection angle at the maximum intensity as a function of photon energy, as shown in Fig. 3G; the shoulder structure is absent at 3 bar, appears at 5 bar, and becomes more obvious when the pressure increases to 8 bar.

The pressure dependence of the shoulder structure suggests that it may be related to the resonant pulse propagation effect [13,34–38]. Most ATAS experiments have assumed that the measured macroscopic absorbance is proportional to the single-atom absorption cross-section and complies with the Beer's law. The treatment implicitly assumes that the absorbing gas is diluted and the transmitted XUV pulse did not change much; such an assumption may not be appropriate at high pressures.

To illustrate this, we first solved the time-dependent Schrödinger equation with a 3-level model. Here, we consider the $1s^2$, $1s2p$, and $1s3s$ states of helium, where the XUV pulse pumps the system from $1s^2$ to $1s2p$, and the residual NIR driving laser couples $1s2p$ and $1s3s$ (Note that in actual experiments, we used 2 silicon mirrors and a 500-μm-diameter pinhole to attenuate the NIR driving laser after high-harmonic generation, which cannot eliminate the NIR pulse completely. An intensity of 2×10^{11} W/cm^2 is estimated for the residual NIR pulse at the sample target based on the Stark shift). We then solved the 1-dimensional Maxwell's wave equation of the XUV pulse in the moving frame ($t' = t - z/c$) in the following:

$$\frac{\partial E_X(t',z)}{\partial z} = -\frac{N}{c\epsilon_0}\frac{\partial \mu(t',z)}{\partial t'}. \quad (2)$$

Here, the induced dipole moments $\mu(t',z)$ resulted from solving the time-dependent Schrödinger equation are inserted as source terms, and the NIR laser is presumptively not changed during its propagation in the gas medium since the absorption of the NIR photon is very weak. The XUV absorption spectrum during propagation is defined by the optical density (OD) in the frequency domain, $OD(\omega,z) = -\log[I(\omega,z)/I_0(\omega)]$, where $I(\omega,z)$ is the intensity of the XUV pulse at distance z, and $I_0(\omega)$ is the input XUV intensity. In our calculations, the intensity of the XUV pulse is 10^{10} W/cm^2, and its duration is 500 as, while the intensity of the 800-nm NIR laser is 2×10^{11} W/cm^2, and its duration is 5 fs. A decay time of 60 fs is used for the laser-induced polarization. The gas pressure of helium is set as 0.8 bar, thus the atomic density $N = 1.9 \times 10^{18}$ atoms/cm^3 at room temperature.

Figure 4A shows the calculated OD. Several reshaping structures were observed, which correspond to multiple subpulses generated during propagation. The characteristic propagation distances where the reshaping structure appears are labeled by white dashed lines. Figure 4C to G shows the XUV envelopes corresponding to $z = 0.02$, 0.04, 0.08, and 0.16 mm, respectively. The initial XUV pulse is short ($z = 0$ mm), and a long

tail (subpulse 1) appears after short propagation ($z = 0.02$ mm), giving rise to the early reshaping of the absorbance. Additional subpulses (2, 3, and 4) appear when the propagation distance increases. These subpulses have different delays with respect to the NIR pulse, causing additional absorption structures. The temporal reshaping of the XUV pulse can be understood as the coherence-induced long tail of the electric field (FID). This newly generated, long-lasting, electric field is out of phase with the driving field, leading to destructive interference (absorption). As the long tail of the electric field propagates through the medium, it in turn will excite new FID (a new subpulse), and the process repeats. Similar results have been previously reported by Liao et al. [13]. We also performed the same calculations without considering the NIR field. Similarly, multiple subpulses were generated in the XUV field, as shown in Fig. 4H to L. These subpulses modify the XUV absorbance, as shown in Fig. 4B. Such modification solely causes a change in absorption strength, while the absorption structure remains as a single peak.

Now, we summarize these observations. Resonant propagation induces temporal reshaping of the XUV pulse, i.e., the formation of subpulses in the XUV time profile. The number of subpulses increases with the propagation distance z, giving rise to several reshaping structures in the absorbance. These subpulses have different delays with the NIR pulse, causing additional absorption structures. In a quantum picture, the XUV pulse excites the coherence between $1s^2$ and $1s2p$ states. The NIR pulse further interacts with the system by coupling $1s2p$ state with $1s3s$ state. Without the NIR pulse, the quantum coherence is limited to $1s^2$ and $1s2p$. The propagation-induced subpulses only modify the absorption spectra in strength. With the NIR pulse, the coherence is further transferred to $1s3s$ state. The evolution of the whole 3-level system modifies the absorption structure; as a result, the single peak structure changes to the doublet peak one.

The Maxwell's wave equation that we used for the propagation calculation is 1-dimensional, and the calculated XUV field only shows information in the propagation direction (z axis). The deflection information, however, is in the angle direction (y axis). To compare with the measured results, we need to simulate the XUV deflection spectrum in the far field. As we described before, such a simulation is based on the small-angle approximation of Kirchhoff diffraction $\tilde{A}(\theta,z=S) \propto \int A(y)e^{i\omega\left[y\sin(\theta)+\frac{y^2}{2S}\right]/c}dy$, $A(y) = A_0(y)e^{\frac{\omega L\{i[n(y)-1]-\beta(y)\}}{c}}$. Although the propagation calculation result elucidates the main effect induced by the resonant pulse propagation, i.e., the XUV subpulse accumulates and strengthens with the propagation distance, resulting in a doublet absorption structure. The distribution information of the real refractive index and the absorption index in the y axis, i.e., $n(y)$ and $\beta(y)$, are missing in such a 1-dimensional (z axis) calculation. Therefore, we cannot use the propagation result directly in the deflection simulation, instead, we used the key idea of a doublet being generated during propagation.

We model the doublet structure by assuming that there are 2 transitions, and they are close to each other in energy. The frequency of transition 1 ($\omega_{0j1} = 21.217$ eV) was chosen based on the energy of $1s^2 \rightarrow 1s2p$ transition of helium. The oscillator strength of transition 1 ($f_{j1} = 0.2764$) was adapted from [32,33]. For transition 2, the resonant frequency ($\omega_{0j2} = \omega_{0j1} + 0.05$ eV) and oscillator strength ($f_{j2} = f_{j1}$) were chosen to form a doublet
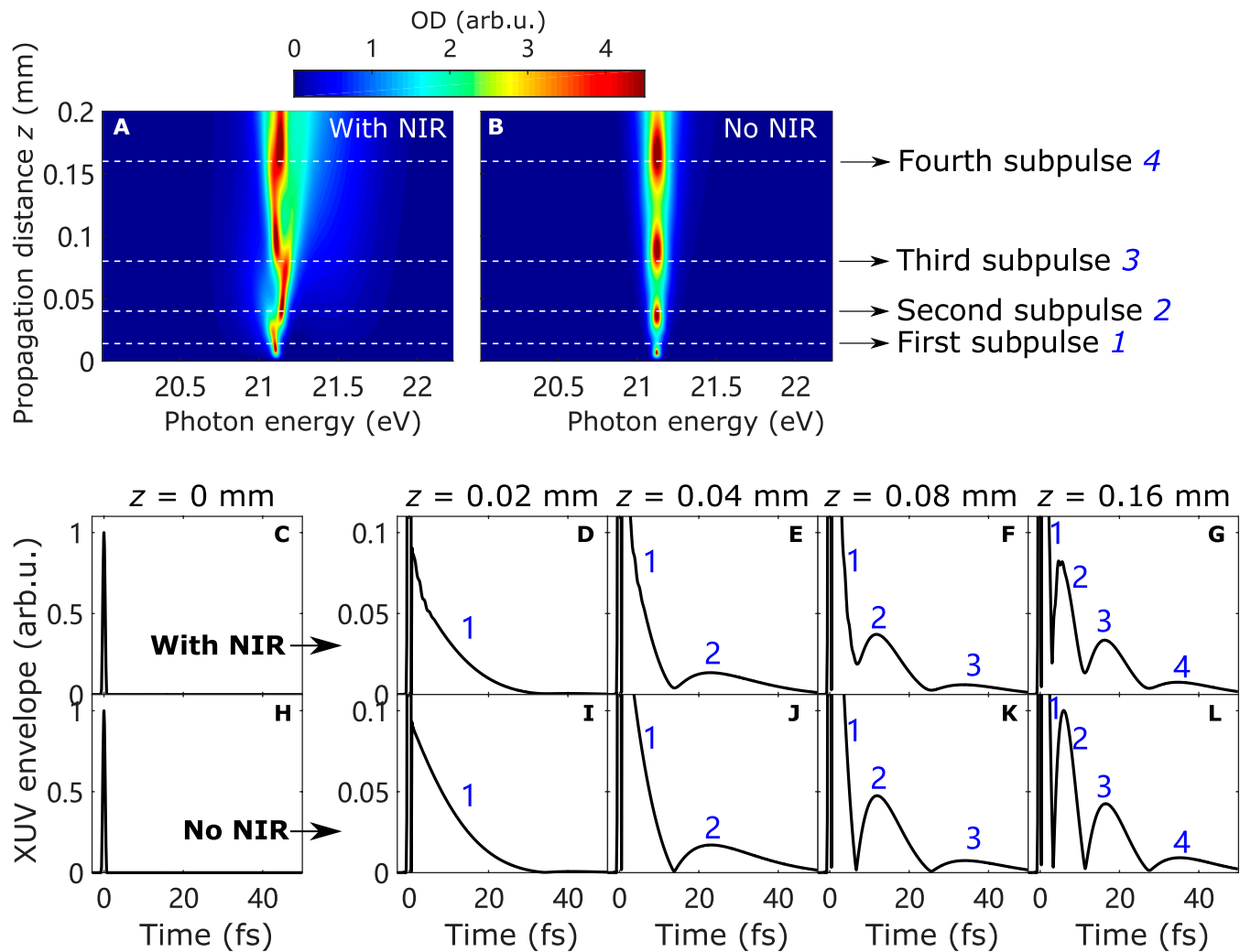
Fig. 4. Propagation calculation of the XUV absorption spectra and XUV envelopes. (A and B) Calculated XUV absorption spectra with/without considering the NIR pulse. Several reshaping structures were observed, which correspond to multiple subpulses generated during propagation. The characteristic propagation distances where the reshaping structure appears are labeled by white dashed lines. (C to G and H to L) The XUV envelopes at $z = 0.02, 0.04, 0.08$, and 0.16 mm with/without considering the NIR pulse. The number of subpulses increases with the propagation distance z.

structure with the same peak height. By using Eq. 1, we calculated the complex refractive index $\tilde{n}$. Figure 5A shows the calculated absorption index β (blue curve) and real refractive index n (red curve). β shows a doublet peak, while n exhibits a shoulder structure between 2 resonance peaks. Figure 5B shows the calculated XUV deflection spectrum for $y = -0.1$ mm (the XUV pulse is 0.1 mm below the gas jet). Similar to the experimental results in Fig. 3C, a narrow feature with small deflection can be seen. Figure 5C shows the XUV spectra after applying intensity normalization along the deflection angle axis, which agrees well with the experimental results in Fig. 3F. We also calculated the deflection spectra by using different ω_{0j2} and f_{j2}; similar shoulder structures were observed as long as a clear doublet structure exists (2 transition peaks with similar intensity are partially overlapped). The effect of a doublet structure was discussed in [14], where the doublet was formed by 4d and 6s resonances (real states) of krypton, and the main discussion of [14] was about the spectrum compression by the 4-wave mixing process. In our case, the doublet was not formed by 2 real states; it was generated during resonant pulse propagation

in helium, and we focused our discussion on the shape of the deflection spectrum.

The shoulder structure observed in the deflection spectra originates from the doublet feature in absorption due to the resonant pulse propagation effect. A comparison between Fig. 5C with the red curve in Fig. 5A shows that the shape of the normalized deflection spectra well reproduces the refractive index line shape. To further illustrate this, we changed the absorption index β line shape from a symmetric Lorentzian profile to an asymmetric Fano profile.

The broadband XUV pulse excites electronic coherences in helium, leading to FID that can last for picoseconds. The temporally overlapped or later-arrived NIR pulse induces an additional phase to the FID, resulting in a different line shape. This additional phase is a cumulative effect that originates from the Stark shift and depends on the delay between the XUV and NIR pulses. We first calculated the transient absorption spectra of helium by using a density matrix approach [39]. Multilevel are considered ($1s^2$, $1s2p$, $1s3s$, $1s3p$, $1s3d$, $1s4s$, $1s4p$, and $1s4d$). The intensity of the XUV pulse is 1×10^{10} W/cm^2, and
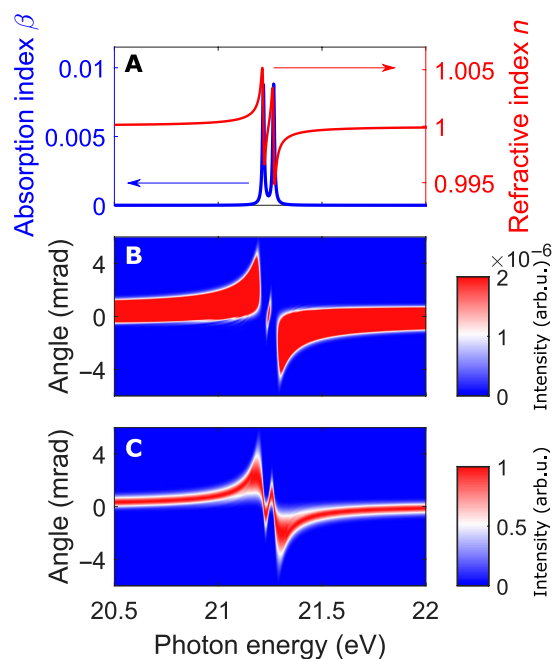
Fig. 5. Calculated XUV deflection spectra by considering a doublet absorption structure. (A) Absorption index β (blue curve) shows that when 2 absorption features are close to each other in energy, the corresponding refractive index n (red curve) exhibits a shoulder structure between 2 resonance peaks. (B) Calculated XUV deflection spectra for $y = -0.1$ mm (the XUV pulse is 0.1 mm below the gas jet). A narrow feature with small deflection can be seen. (C) XUV spectra after applying intensity normalization along the deflection angle axis, the shape of the normalized deflection spectra well reproduces the refractive index line shape. The calculation results agree well with the experimental results in Fig. 3C and F.

its duration is 500 as, while the intensity of the 800-nm control laser is 1×10^{12} W/cm^2, and its duration is 50 fs. Figure 6A shows the calculated delay-dependent absorption spectra, where negative delay means the XUV pulse arrives on the target before the NIR pulse. The main features in Fig. 6A are the ac Stark shift and the laser-induced states, which are well known in ATAS; similar features were observed in [34,38]. For a closer look at the line shape of the 1s2p resonance, we enlarge a portion of Fig. 6A, as shown in Fig. 6B. When the XUV arrival time changes from the rising edge of the NIR pulse (negative delay) to the decreasing edge of the NIR pulse (positive delay), the line shape varies. We chose 4 delays $\tau = 25, 30, -65, -55$ fs (labeled by the white dashed lines in Fig. 6B) to ensure that the XUV pulse arrives at the rising edge or falling edge of the NIR pulse. The corresponding absorbance values are shown in Fig. 6C to F, respectively. The line shapes are asymmetric, i.e., Fano profiles.

For the large negative delays, an additional weak absorption structure exists at the low-energy side of the main Fano profile. Such effect was observed in previous literatures [38] and termed as the sideband formation (the physical mechanism is the later-arrived NIR pulse couples the np states to nearby ns or nd states). We neglect such sideband formation effect since it is much weaker than the main Fano profile. The Fano parameter q changes with the delay, $q \approx 1.7, 3.7, -3.7$, and -1.7 for $\tau = 25, 30, -65$, and -55 fs.

To calculate the deflection spectra, we simulated the absorption index line shape with the Fano parameter $q = 1.7, 3.7, \infty, -3.7$, and -1.7 ($q = \infty$ corresponds to a symmetric Lorentzian profile), as shown by the blue curves in Fig. 7A to E. The red curves are the corresponding refractive index n calculated via
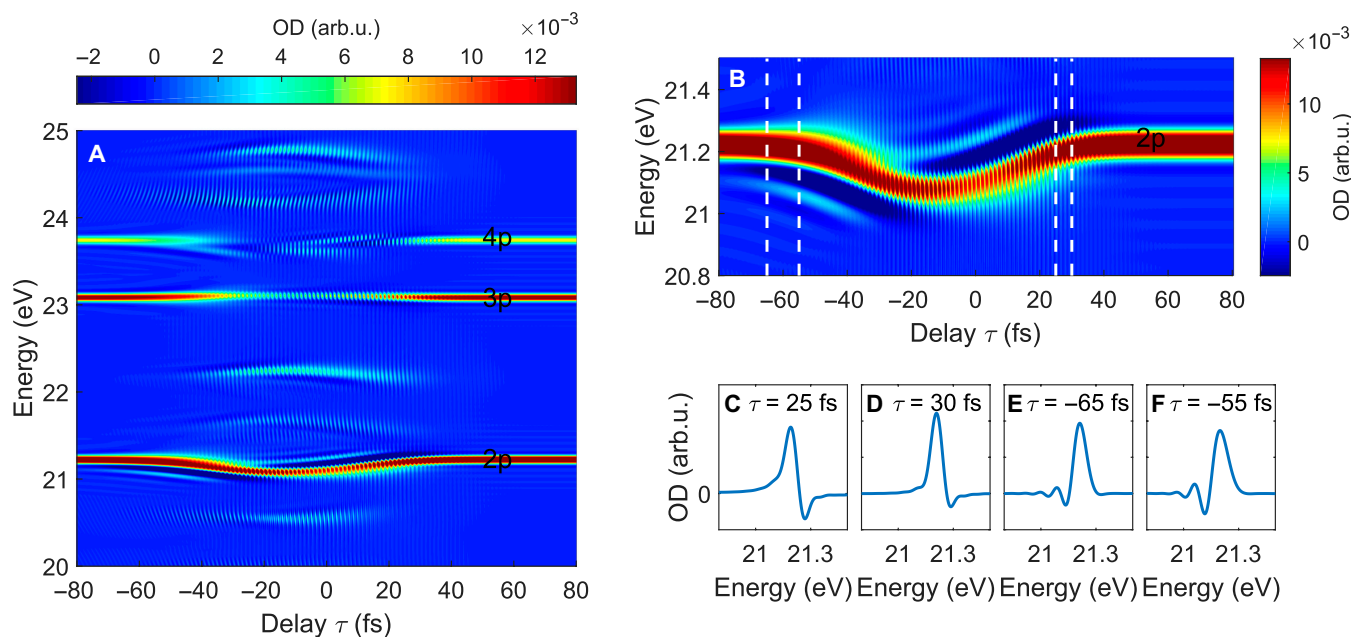
Fig. 6. Calculated delay-dependent absorption spectra of helium. (A) Density matrix calculation of the attosecond transient absorption spectra of helium. The main features are the ac Stark shift and the laser-induced states, which are similar to the results reported in previous literatures. (B) Zoomed-in view of (A). The line shape varies with the delay; 4 delays $\tau = 25, 30, -65$, and -55 fs are chosen (labeled with white dashed lines) to ensure that the XUV pulse arrives at the rising edge or falling edge of the NIR pulse. Negative delay means the XUV pulse arrives on the target before the NIR pulse. (C to F) The absorption spectra corresponding to the 4 chosen delays. The line shapes are asymmetric Fano and the Fano parameters are $q \approx 1.7, 3.7, -3.7$, and -1.7 for $\tau = 25, 30, -65$, and -55 fs.
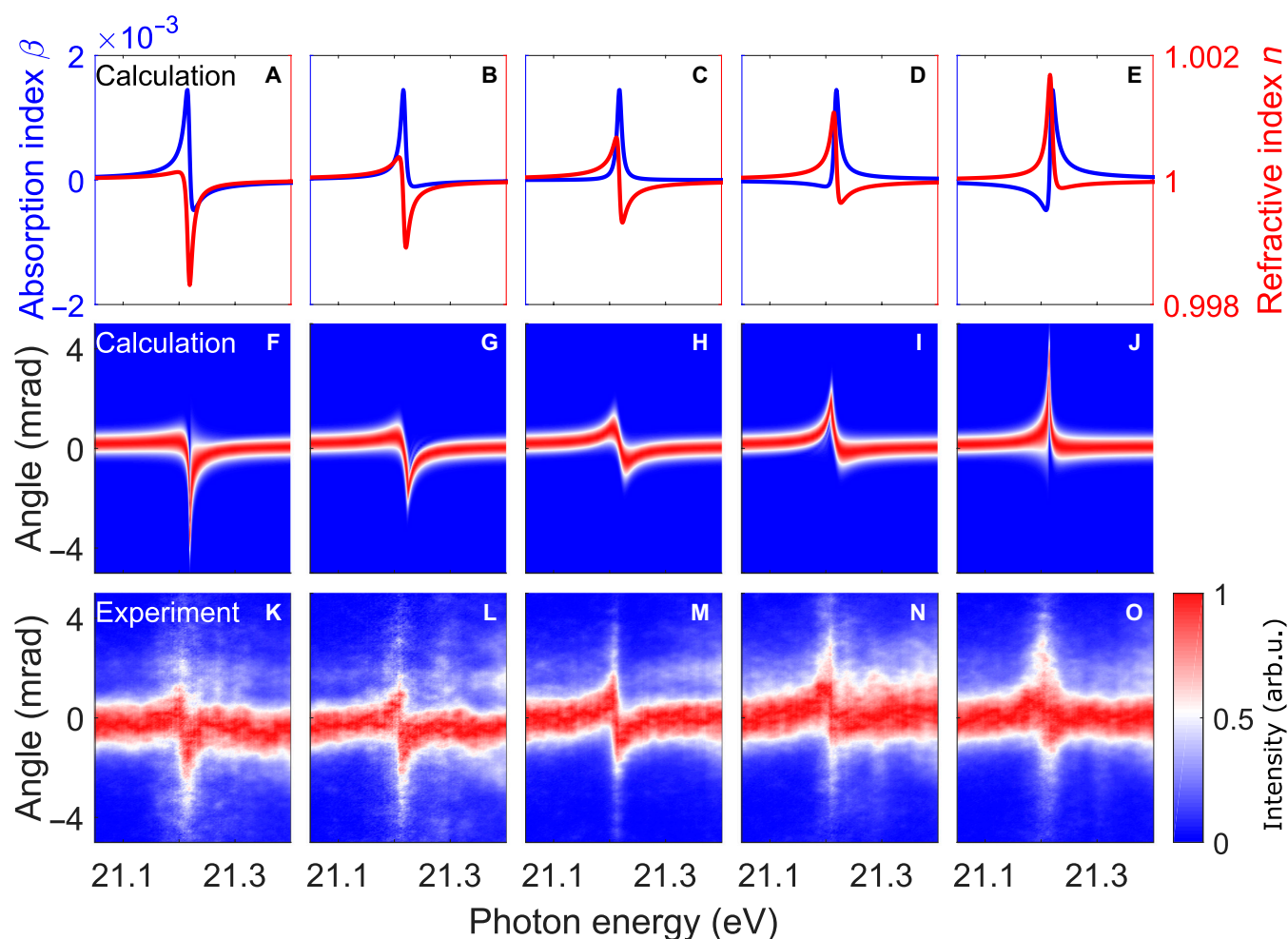
Fig. 7. XUV deflection spectra for different absorption line shapes. (A to E) The absorption index β line shape (blue curve) was changed from a symmetric Lorentzian profile to an asymmetric Fano profile. The corresponding refractive index n (red curve) was calculated via the Kramers–Kronig transform. (F to J) Calculated XUV deflection spectra for $y = -0.1$ mm (the XUV pulse is 0.1 mm below the gas jet). The deflection spectra line shape reproduces the refractive index line shape for all situations. (K to O) The experimentally measured deflection spectra by adding a NIR pulse at different temporal delays. The temporal delays were intentionally selected to ensure that the XUV pulse arrives at the increasing edge or decreasing edge of the NIR pulse. $\tau = 30$ fs for (K), 44 fs for (L), -82 fs for (N), and -36 fs for (O); negative delay means the XUV pulse arrives on the target before the NIR pulse. The NIR pulse was blocked for (M), serving as a reference. The temporally overlapped or later-arrived NIR pulse induces an additional phase to the XUV FID; this additional phase is a cumulative effect that originates from the Stark shift and depends on the delay between the XUV and NIR pulses, resulting in different line shapes. The maximum deflection angle changes from negative to positive, which agrees with the simulation results in (F) to (J).

the Kramers–Kronig transform [29,30]. We assume that the XUV beam is 0.1 mm below the He gas jet; the calculated XUV deflection spectra are shown in Fig. 7F to J. Again, the deflection spectra line shape well reproduces the refractive index line shape for all situations. In the experiments, the temporal delays were intentionally selected to ensure that the XUV pulse arrives at the increasing edge or decreasing edge of the NIR pulse. The delays are respectively 30, 44, -82, and −36 fs for Fig. 7K, L, N and O. The delay points for the simulation [Fig. 6C to F] were chosen to best match the experimental observations. The disparity between the chosen delay values for the simulation and the experiment may arise from 2 reasons. First, the estimated NIR intensity in the simulation is based on the Stark shift, which may be not very accurate. Second, in the adopted multilevel model, the ignored higher levels may affect the 1s2p absorption through the state-coupling effect. Figure 7M shows the XUV deflection spectra when the NIR pulse was blocked. The surface of the aluminum foil was oxidized due to long-term use, and

the low transmission results in a much weaker XUV signal and much more noise. The maximum deflection angle changes from negative to positive, which agrees with the simulation results in Fig. 7F to J very well.

Conclusion

In conclusion, we have investigated the refractive index line shape in ultrafast XUV transient absorption spectroscopy by using the scheme that the XUV pulse traverses the gas jet off-center. The inhomogeneity of the gas jet induces deflection on the XUV radiation, the frequency dependent deflection spectra well reproduce the refractive index line shapes. A typical dispersive refractive index line shape is measured for a single-peak absorption, and an additional shoulder structure with small deflection appears for a doublet absorption. Moreover, the refractive index line shape can be controlled by adding a NIR pulse after the XUV pulse to modify the phase of the FID.

Our results provide a new perspective on studying light–matter interactions by using ultrafast XUV transient absorption spectroscopy. The real refractive index and the absorption index may be measured simultaneously, which provides a full picture of a material's linear response to incident light.

Data Availability

The data that support the findings of this study are available from the corresponding authors upon reasonable request.

References

1. Corkum PB, Krausz F. Attosecond science. *Nat Phys*. 2007;3(6):381–387.
2. Krausz F, Ivanov M. Attosecond physics. *Rev Mod Phys*. 2009;81(1):163–234.
3. Peng P, Marceau C, Villeneuve DM. Attosecond imaging of molecules using high harmonic spectroscopy. *Nat Rev Phys*. 2019;1:144–155.
4. Kraus PM, Zürch M, Cushing SK, Neumark DM, Leone SR. The ultrafast X-ray spectroscopic revolution in chemical dynamics. *Nat Rev Chem*. 2018;2:82–94.
5. Huang Y, Zhao J, Shu Z, Zhu Y, Liu J, Dong W, Wang X, Lü Z, Zhang D, Yuan J, et al. Ultrafast hole deformation revealed by molecular attosecond interferometry. *Ultrafast Sci*. 2021;2021:Article 9837107.
6. Guan M, Chen D, Hu S, Meng S. Theoretical insights into ultrafast dynamics in quantum materials. *Ultrafast Sci*. 2022;2022:Article 9767251.
7. Goulielmakis E, Loh Z-H, Wirth A, Santra R, Rohringer N, Yakovlev VS, Zherebtsov S, Pfeifer T, Azzeer AM, Kling MF, et al. Real-time observation of valence electron motion. *Nature*. 2010;466:739–743.
8. Ott C, Kaldun A, Raithet P, Meyer K, Laux M, Evers J, Keitel CH, Greene CH, Pfeifer T. Lorentz meets Fano in spectral line shapes: A universal phase and its laser control. *Science*. 2013;340(6133):716–720.
9. Kaldun A, Blättermann A, Stooß V, Donsa S, Wei H, Pazourek R, Nagele S, Ott C, Lin CD, Burgdörfer J, et al. Observing the ultrafast buildup of a Fano resonance in the time domain. *Science*. 2016;354(6313):738–741.
10. Pertot Y, Schmidt C, Matthews M, Chauvet A, Huppert M, Svoboda V, von Conta A, Tehlar A, Baykusheva D, Wolf J-P, et al. Time-resolved x-ray absorption spectroscopy with a water window high-harmonic source. *Science*. 2017;355(6322):264–267.
11. Kobayashi Y, Chang KF, Zeng T, Neumark DM, Leone SR. Direct mapping of curve-crossing dynamics in IBr by attosecond transient absorption spectroscopy. *Science*. 2019;365(6448):79–83.
12. Loh Z-H, Doumy G, Arnold C, Kjellsson L, Southworth SH, Al Haddad A, Kumagai Y, Tu M-F, Ho PJ, March AM, et al. Observation of the fastest chemical processes in the radiolysis of water. *Science*. 2020;367(6474):179–182.
13. Liao C-T, Sandhu A, Camp S, Schafer KJ, Gaarde MB. Beyond the single-atom response in absorption line shapes: Probing a dense, laser-dressed helium gas with attosecond pulse trains. *Phys Rev Lett*. 2015;114(14):Article 143002.
14. Drescher L, Kornilov O, Witting T, Shokeen V, Vrakking MJJ, Schütte B. Extreme-ultraviolet spectral compression by four-wave mixing. *Nat Photonics*. 2021;15:263–266.
15. Chini M, Zhao B, Wang H, Cheng Y, Hu SX, Chang Z. Subcycle AC Stark shift of helium excited states probed with isolated attosecond pulses. *Phys Rev Lett*. 2012;109(7): Article 073601.
16. Chini M, Wang X, Cheng Y, Wu Y, Zhao D, Telnov DA, Chu S-I, Chang Z. Sub-cycle oscillations in virtual states brought to light. *Sci Rep*. 2013;3:Article 1105.
17. Reduzzi M, Hummert J, Dubrouil A, Calegari F, Nisoli M, Frassetto F, Poletto L, Chen S, Wu M, Gaarde MB, et al. Polarization control of absorption of virtual dressed states in helium. *Phys Rev A*. 2015;92(3):Article 033408.
18. Cao W, Warrick ER, Fidler A, Leone SR, Neumark DM. Excited-state vibronic wave-packet dynamics in H_2 probed by XUV transient four-wave mixing. *Phys Rev A*. 2018;97(2):Article 023401.
19. Hosler ER, Leone SR. Characterization of vibrational wave packets by core-level high-harmonic transient absorption spectroscopy. *Phys Rev A*. 2013;88(2):Article 023420.
20. Wei Z, Li J, Wang L, See ST, Jhon MH, Zhang Y, Shi F, Yang M, Loh ZH. Elucidating the origins of multimode vibrational coherences of polyatomic molecules induced by intense laser fields. *Nat Commun*. 2017;8:Article 735.
21. Peng P, Mi Y, Lytova M, Britton M, Ding X, Naumov AY, Corkum PB, Villeneuve DM. Coherent control of ultrafast extreme ultraviolet transient absorption. *Nat Photonics*. 2022;16:45–51.
22. Peng P, Marceau C, Hervé M, Corkum PB, Naumov AY, Villeneuve DM. Symmetry of molecular Rydberg states revealed by XUV transient absorption spectroscopy. *Nat Commun*. 2019;10:Article 5269.
23. Kaldun A, Ott C, Blättermann A, Laux M, Meyer K, Ding T, Fischer A, Pfeifer T. Extracting phase and amplitude modifications of laser-coupled Fano resonances. *Phys Rev Lett*. 2014;112(10):Article 103001.

24. Drescher L, Kornilov O, Witting T, Reitsma G, Monserud N, Rouzée A, Mikosch J, Vrakking MJJ, Schütte B. Extreme-ultraviolet refractive optics. *Nature*. 2018;564:91–94.

25. Attar AR, Bhattacherjee A, Pemmaraju CD, Schnorr K, Closser KD, Prendergast D, Leone SR. Femtosecond x-ray spectroscopy of an electrocyclic ring-opening reaction. *Science*. 2017;356(6333):54–59.

26. Wu M, Chen S, Camp S, Schafer KJ, Gaarde MB. Theory of strong-field attosecond transient absorption. *J Phys B Atomic Mol Phys*. 2016;49(6):Article 062003.

27. Hammond TJ, Monchocé S, Zhang C, Vampa G, Klug D, Naumov AY, Villeneuve DM, Corkum PB. Integrating solids and gases for attosecond pulse generation. *Nat Photonics*. 2017;11:594–599.

28. Hammond TJ, Villeneuve DM, Corkum PB. Producing and controlling half-cycle near-infrared electric-field transients. *Optica*. 2017;4(7):826–830.

29. Lucarini V, Peiponen K, Saarinen JJ, Vartiainen EM. *Kramers-Kronig relations in optical materials research*. New York (NY): Springer; 2005.

30. Boyd RW. *Nonlinear optics*. Rochester (US): Academic Press; 2008.

31. Born M, Wolf E, Bhatia AB, Clemmow PC, Gabor D, Stokes AR, Taylor AM, Wayman PA, Wilcock WL. *Principles of Optics 7th expanded edn*. Cambridge (UK): Cambridge Univ. Press; 1999.

32. Wiese WL, Smith MW, Glennon BM. Atomic Transition Probabilities: Hydrogen through Neon. Technical report, National Standard Reference Data System (NBS, 1966).

33. Wiese WL, Smith MW, Glennon BM. Atomic Transition Probabilities: Sodium through Calcium. Technical report, National Standard Reference Data System (NBS, 1969).

34. Chen S, Wu M, Gaarde MB, Schafer KJ. Laser-imposed phase in resonant absorption of an isolated attosecond pulse. *Phys Rev A*. 2013;88(3):Article 033409.

35. Pfeiffer AN, Bell MJ, Beck AR, Mashiko H, Neumark DM, Leone SR. Alternating absorption features during attosecond-pulse propagation in a laser-controlled gaseous medium. *Phys Rev A*. 2013;88(5):Article 051402.

36. Gaarde MB, Buth C, Tate JL, Schafer KJ. Transient absorption and reshaping of ultrafast XUV light by laser-dressed helium. *Phys Rev A*. 2011;83(1):Article 013419.

37. Chu WC, Lin CD. Resonant enhancement of a single attosecond pulse in a gas medium by a time-delayed control field. *J Phys B Atomic Mol Phys*. 2012;45:Article 201002.

38. Wu M, Chen S, Schafer KJ, Gaarde MB. Ultrafast time-dependent absorption in a macroscopic three-level helium gas. *Phys Rev A*. 2013;87(1):Article 013828.

39. Pfeiffer AN, Leone SR. Transmission of an isolated attosecond pulse in a strong-field dressed atom. *Phys Rev A*. 2012;85(5):Article 053422.